1644 *Macromolecules* **2010**, *43*, 1644–1650
DOI: 10.1021/ma9023203

Macromolecules
ARTICLE

Ordering Dynamics of Directed Self-Assembly of Block Copolymers in Periodic Two-Dimensional Fields

Weihua Li,*,†,‡ Feng Qiu,*,†,‡ Yuliang Yang,†,‡ and An-Chang Shi§

†*The Key Laboratory of Molecular Engineering of Polymers, Ministry of Education, China,* ‡*Department of Macromolecular Science, Fudan University, Shanghai 200433, China, and* §*Department of Physics and Astronomy, McMaster University, Hamilton, Ontario, Canada, L8S 4M1*

Received October 19, 2009; Revised Manuscript Received November 28, 2009

ABSTRACT: The ordering dynamics of directed self-assembly of cylinder-forming diblock copolymers is studied by cell dynamics simulations. The directing field, mimicking chemically or topologically patterned substrates, is in the form of hexagonally arranged potential wells attractive to minority blocks. Time evolution of the defect concentration is used to characterize the ordering dynamics of the self-assembled cylindrical structures of the block copolymers. When the period of the external potential, L_s, is a small integer multiple of the cylinder-to-cylinder distance, L_0, of the block copolymer microphase, the defect concentration decays exponentially. The defect annihilation becomes slower as L_s is increased, and eventually, the exponential decay law is broken. When the ratio L_s/L_0 is a square root of an integer, large polycrystalline grains with different orientations are observed. The results are consistent with available experimental and theoretical results.

I. Introduction

The self-assembly of block copolymers (BCPs) as a potential candidate of functional materials has received tremendous attention in recent years.[1−8] In semiconductor technology, standard photolithography is becoming expensive for the manufacturing of sub-30-nm patterns as it approachs the intrinsic technological limits. The demand for higher-density features for improved data storage and computing speed makes researchers turn to the self-assembly of BCPs, which spontaneously form periodic patterns on the length scale of nanometers. Even for the simplest BCPs, diblock copolymer, lamellar, gyroidal, cylindrical, and spherical microstructures can form by tuning the relative composition of the two blocks.[9] Lithography in practical applications of high-performance functional materials requires long range of order, very low density of defects, and uniform domain shapes. Unfortunately, the perfect periodic domain ordering is usually destroyed by the appearance of defects. For example, the grain boundary between lamellae with mismatch orientations usually appears in the lamellar phase; the defects of dislocation and disclinations can destroy the translational and orientational order in thin films of hexagonally arranged cylinders (or spheres) formed by BCPs. Vinals and coworker have performed a series of research on grain boundary dynamics and defect dynamics in bulk lamellar phase.[11−13] The study of both experiments[10,14,15] and computer simulations[16,17] shows that the orientation correlation length grows with time according to a power law with an exponent of 1/4 in cylinder- or sphere-forming system. Therefore, for macroscale thin films (from micrometers to millimeters) on an uniform substrate, the relaxation time to annihilate all defects is infinitely long. Additional techniques are required to obtain improved ordering in BCP films.

A wide range of techniques, including shear,[18] electric fields,[3] thermal gradients,[19,20] solvent annealing,[21] flow,[22] graphoepitaxy,[23−25] and chemical prepatterning,[26,27] has emerged to improve the order of the self-assembly microstructures in BCP films. For example, Kim et al. obtained PS-*b*-PMMA lamellar structures with a long-range order under the direction of chemical-prepatterned substrates.[26] In this prepatterning method, it is disadvantageous that the substrate patterns have a very close period with the natural period of lamellar structure, which challenges the e-beam lithography. Recently, a significant progress has been made using the graphoepitaxial techniques to induce higher degrees of ordering perfection. Ruiz et al. developed a directed assembly method with which the self-assembly of BCPs can be used to interpolate the chemical patterns and rectify the pattern quality.[28] With the interpolation of chemical patterns, one only needs to produce a sparser pattern of round spots with an e-beam than the microdomain array itself. With similar techniques, Cheng et al. obtained an interpolation for lamellar structures with up to four times the period of the lamellae;[29] Tada et al. did a careful study on the interpolating effect for length ratio of chemical-pattern spacing to the period of BCPs and other conditions.[30] Their results show that the interpolating effect is sensitive to the length ratio. When the length ratio slightly deviates from an integer multiple (such as −5 or +10%), small density of dislocation or disclination defects can form. Bita et al. demonstrate another effective graphoepitaxial method to direct the self-assembly of BCP thin films.[32] They use sparse arrays of posts to induce graphoepitaxially long-range order of hexagonally packed spheres formed by PS-*b*-PMMA BCPs. The carefully designed posts, which are chemically and physically nearly distinguishable, act as surrogate spherical or cylindrical domains of the minority of the BCP. Extremely high degrees of translational and orientational order are achieved when the length ratio of the post-to-post distance to the BCP domain spacing varies from 1.65 to 4.6 multiples.

Theoretical research on the graphoepitaxial method to direct the self-assembly of BCP thin films is very limited, although many experiments have been carried on this topic. A Monte Carlo simulation was carried to study the self-assembly of cylinder-forming diblock copolymers on chemically nanopatterned substrates with

*Corresponding author. E-mail: weihuali@fudan.edu.cn (W.L.); fengqui@fudan.edu.cn (F.Q.).

 Published on Web 01/13/2010

hexagonal, stripe, and square patterns by Wang et al.[33] Long-range ordering can be achieved when two conditions are satisfied: a lower hexagonally patterned substrate and commensurate pattern spacing with the period of the cylinder-domain array. Edwards et al. did a single-chain-in-mean-field simulations to investigate the formation of lamellae directed by strip-patterned substrate.[34] To the best of our knowledge, the study on the ordering dynamics of the graphoepitaxially directed assembly of BCP thin films is lacking. The knowledge of the ordering dynamics is helpful to understand the self-assembling mechanism of BCPs on the chemical or physical nanopatterned substrates; therefore, it can help experiments to develop more efficient techniques

In this work, we investigate the microdomain ordering dynamics directed by a 2D hexagonal array of round chemical-potential wells in cylinder-forming diblock copolymer thin films. The potential wells, with center-to-center distance of L_s, have a preferential interaction with the minority block of the BCPs. The commensurability parameter, L_s/L_0, where L_0 is the cylinder-to-cylinder distance of the diblock copolymers in bulk, is the main factor that influences the degree of ordering perfect. To focus on the influence of the length ratio parameter L_s/L_0 on the ordering dynamics, we simplify the thin films to a 2D system with a translational symmetry normal to the surface. This simplification, which neglects the effect of the thickness of the films, can be applied to experimental systems with appropriate film thickness and field strength where perpendicular cylinders are formed on the substrate.[30,31] To make our simulation results comparable to experimental results, we consider a system size as large as micrometers by micrometers, where more than 10 000 domains form.

Simulation of large systems is enabled by the application of cell dynamics method. The cell dynamics simulation (CDS) method based on the time-dependent Ginzburg−Landau (TDGL) equation has been used extensively to simulate phase separation dynamics because it was introduced to the study of phase separation of polymer blends and diblock copolymers by Oono and coworkers.[35−37] The CDS method applies a coarse-grained discretization of the TDGL equation. The time evolution of the order parameter, which is the volume fraction of one component in the diblock copolymer microphase separations, is evaluated on a lattice according to the local driving force due to chemical potential gradients and the diffusive dynamics from order parameter variations in neighboring cells. The CDS method has high computational efficiency compared with other dynamical simulation methods, such as dissipative particle dynamics simulations[38] and dynamic density functional simulations.[39] Therefore, it is suitable to study such large system.

II. Model and Theory

We consider an incompressible asymmetric AB diblock copolymers with equal monomer size. Each copolymer has identical volume fraction $f = 0.35$ of A block. A hexagonally arranged cylindrical phase can form when microphase separation occurs. The dynamics of microphase separation for diblock copolymers can be described by the following TDGL equation for a conserved order parameter[36]

$$\frac{\partial \phi}{\partial t} = M\nabla^2 \frac{\partial F[\phi]}{\partial \phi} + \eta(\mathbf{r}, t) \tag{1}$$

where the order parameter ϕ is chosen as the local composition difference between A and B components, M is a phenomenological mobility coefficient, set as $M = 1$, $F[\phi]$ is the free energy functional for diblock copolymers, and $\eta(\mathbf{r}, t)$ is a random noise term, with zero average and a second moment of

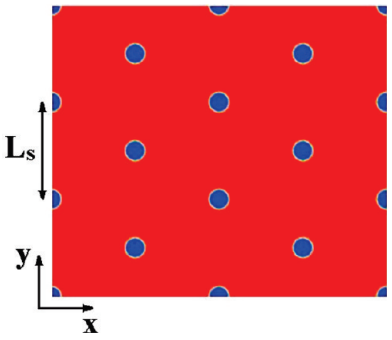

Figure 1. Schematic plot of the hexagonal array of the potential wells. The blue color indicates the regions where the minority block is preferred, and the red regions do not have preference to both block. L_s gives the center-to-center distance of the potential wells. The periods along x and y directions are $\sqrt{3}L_s$ and L_s, respectively.

$\langle \eta(\mathbf{r}, t)\eta(\mathbf{r}', t')\rangle = -\eta_0 M\nabla^2\, \delta(\mathbf{r}-\mathbf{r}')\, \delta(t-t')$; here η_0 is the noise strength. The free energy functional $F[\phi]$ includes a short-range term and a long-range term. After introducing an external field, $H_{ext}(\mathbf{r})$, the expression of $F[\phi]$ can be written as

$$F[\phi] = F_{GL}[\phi] + \frac{\alpha}{2}\int d\mathbf{r} \int d\mathbf{r}'\, G(\mathbf{r}-\mathbf{r}')\, \delta\phi(\mathbf{r})\, \delta\phi(\mathbf{r}') + \int d\mathbf{r}\, H_{ext}(\mathbf{r})\phi(\mathbf{r}) \tag{2}$$

where $\delta\phi(\mathbf{r}) = \phi(\mathbf{r}) - \bar{\phi}$, and $\bar{\phi} = 2f-1$ is the average value of $\phi(\mathbf{r})$ over the 2D space. The first term can be modeled by a Ginzburg−Landau free-energy functional[40]

$$F_{GL}[\phi] = \int d\mathbf{r} \left[\frac{1}{2}(\nabla\phi)^2 + W(\phi)\right] \tag{3}$$

where $W(\phi)$ is the local contribution of the interaction. According to the functional derivative in eq 1, one needs the derivative of $W(\phi)$. We choose $W(\phi)$ as

$$\frac{dW}{d\phi} = -A\tanh(\phi) + \phi \tag{4}$$

with $A = 1.3$. The second term of expression 2 with a positive constant α results in a long-range repulsive interaction and is inherent to microphase separation. Therefore α is the main factor influencing the characteristic wavelength, that is, the cylinder-to-cylinder distance of L_0 in our system. Larger α gives smaller L_0. Small L_0 indicates less points for each microdomain when the grid spacing is fixed. However, large L_0 reduces the number of microdomains for fixed lattice sizes. To keep L_0 reasonable for our simulations, we choose $\alpha = 0.02$. For the case of diblock copolymers, the form of $G(\mathbf{r}-\mathbf{r}')$ can be expressed as[41]

$$-\nabla^2 G(\mathbf{r}-\mathbf{r}') = \delta(\mathbf{r}-\mathbf{r}') \tag{5}$$

After inserting eqs 2−5, the dynamic equation becomes

$$\frac{\partial \phi}{\partial t} = \nabla^2\{-M\nabla^2\phi(\mathbf{r}, t) - A\tanh[\phi(\mathbf{r}, t)] + \phi(\mathbf{r}, t) + H_{ext}(\mathbf{r})\} - \alpha\, \delta\phi(\mathbf{r}, t) + \eta(\mathbf{r}, t) \tag{6}$$

According to the chemical patterns made by experiments,[28,30] we choose a hexagonally arranged array of external potential wells with center-to-center distance of L_s (schematic Figure 1), which is typically larger than the period L_0 of diblock copolymers.

The potential around these blue spots is chosen to be a hyperbolic tangent form

$$H_{ext}(\mathbf{r}) = -\frac{1}{2}V_0\{\tanh[(-|\mathbf{r}-\mathbf{R}_i|+\sigma)/\lambda]+1\} \quad (7)$$

for $|\mathbf{r}-\mathbf{R}_i| \le 2\sigma$ and otherwise $H_{ext}(\mathbf{r}) = 0$ (the red area in Figure 1). In the above expression of the potential, a positive value of V_0 gives the strength of the field, which is preferential to minor A block. The magnitude of V_0 determines how much A component is attracted to the potential-well areas. Too small V_0 can not influence the self-assembling of cylinders. In our simulations, $V_0 = 0.04$ is large enough to direct a long-range order of cylinders for appropriate L_s/L_0. When $V_0 = 0$, the system is reduced to the thin films on a uniform substrate. $\mathbf{R}_i$ indicates the position center of potential well i, and σ characterizes the radial size of the well. The diameter of the well with field strength $H_{ext} = -V_0/2$ is 2σ. The value of σ is set as $0.15L_0$, which is comparable to the size of the cylinders in bulk. The parameter of $\lambda = 0.5$ gives the steepness of the potential near the well edge. Smaller value of λ corresponds to steeper potential change at the well edge. The potential form is cylindrically symmetric in the 2D film surface and is invariant along the normal direction of the film for each well.

Here we adopt the notation of the form $\langle ij\rangle$ to characterize the multiplying property of the periodic field as ref 32 does, with which the basis vector of the potential-well lattice is equal to the sum of integer multiples i and j of the two 60°-oriented basis vectors of the BCP microdomain lattice. The ratio of L_s/L_0 can be readily determined as $(i^2 + j^2 + ij)^{1/2}$, and the angle θ, which describes the relative orientation of the BCP microdomain lattice to the potential-well lattice, is given by

$$\theta = \arccos\left(\frac{2i+j}{2\sqrt{i^2+j^2+ij}}\right) \quad \text{or}$$

$$\theta = -\arccos\left(\frac{2i+j}{2\sqrt{i^2+j^2+ij}}\right) \quad (8)$$

The positive and negative angles refer to two relative orientations. When one of i and j is zero (such as $\langle 20\rangle$, $\langle 30\rangle$, $\langle 40\rangle$, and so on), L_s is an integer multiple of L_0, and the absolute value of θ is 0 or 60°. Consequently, positive and negative angles are equivalent for hexagonal lattices, and both of them indicate that the potential-well lattice and the microdomain lattice have consistent orientation. Otherwise, when $i \neq j$, L_s is a square root of an integer multiple of L_0, and the absolute value of θ is between 0 and 60°. In this case, the two angles give two different relative orientations. For example, for $<21>$, $L_s/L_0 = \sqrt{7}$ and $\theta \approx \pm 19.1°$. For this potential-well lattice, two possible orientations of the BCP microdomain lattices can appear simultaneously to form polycrystalline arrays, which have been observed by experiments.[32]

In our simulations, the 2D film is divided into a $N_x \times N_y$ grid with unit cell size of $\Delta_x = \Delta_y = 1$. The values of N_x and N_y are determined by $N_x = \sqrt{3}n_x^s L_s$ and $N_y = n_y^s L_s$, where n_x^s and n_y^s are the period numbers of the potential-well array along the x and y directions ($n_x^s = 3$ and $n_y^s = 2$ in Figure 1). To keep the system size large enough to form $>10^4$ cylinders (including the spots themselves), n_x^s and n_y^s are chosen to ensure that either N_x or N_y is >850 in all simulations. For the case of $V_0 = 0$, fixed $N_x = 1024$ and $N_y = 1024$ are used. Periodic boundary conditions are imposed on the simulated rectangle box. Following the discretization scheme in the cell dynamics,[35,37] the Laplacian is replaced by the average

$$\nabla^2 X \approx \frac{1}{6}\sum_{n.n} X + \frac{1}{12}\sum_{n.n.n} X - X \quad (9)$$

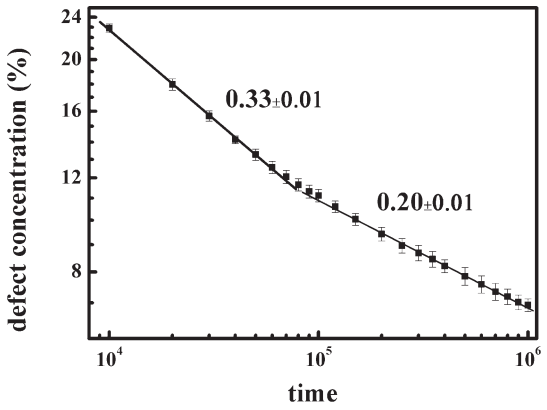

Figure 2. Time evolution of the defect concentration for the case of uniform substrate. Two solid lines correspond to the best-fit power laws for short- and long-time processes.

where *n.n* (*n.n.n*) means the summation over the (next-) nearest-neighbor cells. Initially, we put the system in a high-temperature uniform state by initializing the order parameter with small random fluctuations in the simulations. At $t = 0$, we quench the system below the phase-separation temperature.

III. Results and Discussion

To set an appropriate value of L_s relative to L_0, we first need to estimate L_0 for the chosen parameters of the diblock copolymers. L_0 can be determined by the position of the main peak of the circularly averaged scattering function $kS(k, t)$ for diblock copolymer thin films on an uniform substrate of $V_0 = 0$. The lattice constant is determined to be $L_0 = 9.20$ in our simulations. In the literature,[15−17] the orientational correlation length ξ_6, defined by the roughly exponential decay of the orientational correlation function $g_6(r, t)$, is used to measure the ordering dynamics of cylinder-forming diblock copolymers. Here we use an alternative quantity, the defect concentration, to characterize the ordering dynamics. There are two reasons for this choice. One is that the number of defects can be calculated directly from the density profiles for required time steps, and it is complementary to the correlation/orientational−correlation length in describing the ordering degree. The second reason is that the ordering process of the microdomain arrays after being imposed by the field pattern becomes much faster than that in bulk, and in consequence, the orientational correlation function has larger fluctuations for the case of low defect concentration. It is difficult to determine the orientational correlation length from the process of data-fitting. Although large fluctuations definitely appear in the results of the defect number as well, we can conveniently estimate its error by statistical method, and control it within the acceptable range by increasing statistical samples. The defect concentration as a function of time is defined as $f_{DF}(t) = n_{DF}(t)/n_{MD}(t) \times 100\%$, where $n_{DF}(t)$ and $n_{MD}(t)$ are the total number of defects and microdomains at time t, respectively. The function of $f_{DF}(t)$ is calculated by averaging data on 8−16 independent simulated samples. More samples are simulated to collect data for the systems with lower defect concentrations; for example, 16 samples are used in the case of $L_s/L_0 = 3$.

As a reference of the results of $V_0 \neq 0$, the temporal evolution of the defect concentration, obtained from the density profiles in the case of uniform substrate, is shown in Figure 2, and three typical density profiles and the corresponding profiles of their orientational order parameter $\psi(\mathbf{r})$, which is defined as $\psi(\mathbf{r}) = \exp[6i\theta(\mathbf{r})]$ where $\theta(\mathbf{r})$ is the local interdomain "bond" orientation,[15,16,42] are shown in Figure 3. For the reason of clarity, 1/4 of the area of the whole 1024×1024 region is shown. There are two main steps during the standard data processing: calculating the

vertex of each microdomain and conducting the Delaunay triangulation with these vertexes.[16] With the Delaunay triangles, the defects can be readily collected by the rule that the number of their connected bonds is not equal to six. That most of defects have five or seven coordinated cylinders in our results is consistent with the observations of the literatures.[15,16] When collecting the data of defects, we do not distinguish five, seven, or other coordinated-cylinder defects, and only the total number of defects is recorded. The error bars of the data in the evolution function of defects is obtained by averaging on eight independent simulated samples. Similar properties of defects and grains, which have been carefully discussed in refs 15 and 16, can be seen in our results. For example, a line of dislocations delimiting two grains with a large-angle grain boundary (the largest red grain and its right neighbor green grain in the bottom-right figure) has been observed. From the double-logarithmic plot of Figure 2, we can see that there are two evolution stages. The defect concentration as a function of time obeys a power law $f_{DF}(t) \approx t^{1/3}$ for the time shorter than 10^5 and $f_{DF}(t) \approx t^{1/5}$ for the time from 10^5 to 10^6. A similar two-stage dynamic process has also been seen in ref 42. The short-time behavior can be understood by the coarse-graining mechanism that small domains are absorbed by larger domains.[43] The exponent of 1/5 for the long-time dynamics is consistent with the results in the literature.[15,16,42] They found exponents of about 1/5 for the correlation length $\xi_S(t)$ and 1/4 for the orientational correlation length $\xi_6(t)$. Details about the coarsening process in this term can be found in the literature.[15,16] The defect concentrations for the density plots at $t = 10^4$, 10^5, and 10^6 in Figure 3 are (22.9 ± 0.4), (11.1 ± 0.3), and (6.9 ± 0.2)%, respectively.

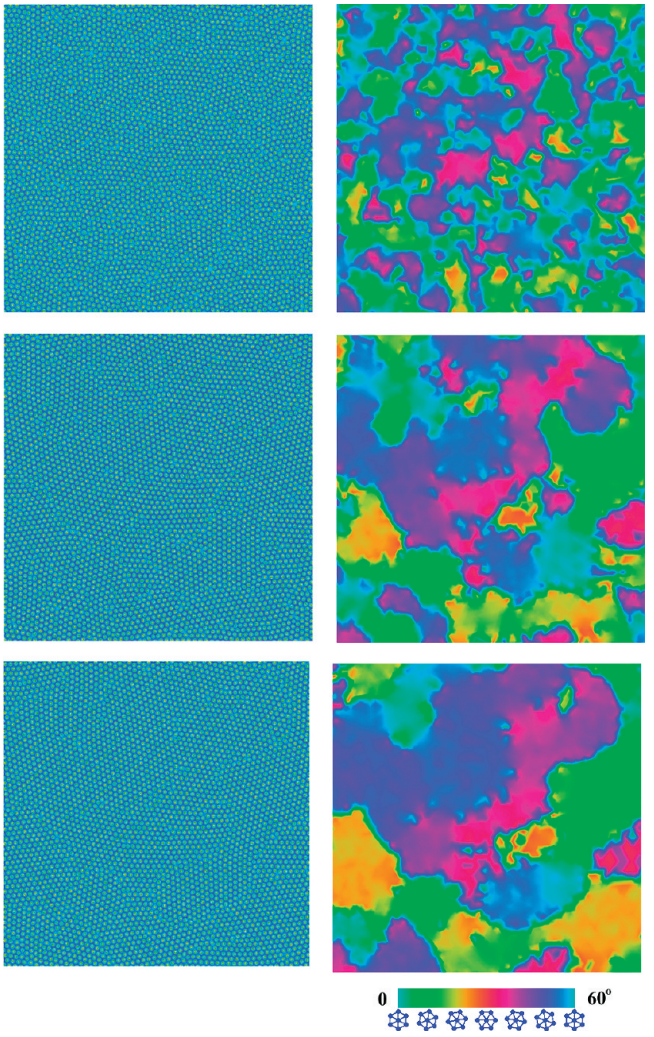

Figure 3. Typical monomer density plots (left column) and corresponding distribution maps (right column) of local lattice orientation where the colors of the spectrum indicate a range from 0 to 60°. For the monomer density plots, light-red (or yellow) color indicates high density of the minority block. From top to bottem, the time is $t = 10^4$, 10^5, and 10^6, respectively.

First, we examine the BCP self-assembly on the field-patterned substrate with field patterns of $\langle i0 \rangle$, where $L_s/L_0 = i$. The defect concentrations as a function of time for $i = 3$, 4 and $i = 5$, 6 are plotted in Figure 4a,b, respectively. The parameters of the lattice are $(n^s_x, n^s_y, N_x, N_y) = (20, 32, 956, 883)$ for $\langle 30 \rangle$, $(n^s_x, n^s_y, N_x, N_y) = (15, 24, 956, 883)$ for $\langle 40 \rangle$, $(n^s_x, n^s_y, N_x, N_y) = (12, 20, 956, 920)$ for $\langle 50 \rangle$, and $(n^s_x, n^s_y, N_x, N_y) = (10, 16, 956, 883)$ for $\langle 60 \rangle$. The results for $\langle 30 \rangle$, $\langle 40 \rangle$, $\langle 50 \rangle$, and $\langle 40 \rangle$, are obtained by averaging on 16, 10, 8, and 8 samples, respectively. As the defects are annihilating, the fluctuation of the number of defects becomes large, and in consequence, the relative error becomes large. We can estimate the real size of the simulated box by relating L_0 to that of some experimental data. For example, $L_0 = 40$ nm in ref 32 (PMDS sphere-to-sphere distance in PS matrix), and the lattice of $N_x \times N_y = 956 \times 883$ with $L_0 = 9.20$ lattice corresponds to a real size of about $4.1 \times 3.4\,\mu m^2$. It is larger than the typical size $2\,\mu m$ of the defect-free arrays observed in experiments.[32] The logarithmic linear plot of Figure 4a suggests that the defect concentrations for $\langle 30 \rangle$ and $\langle 40 \rangle$ have an exponential decay with time, which is substantially faster than that on the uniform substrate. Apparently, the process of the defect annihilation becomes slow as the field-spot lattice becomes sparse. For $\langle 30 \rangle$, a pefect order of microdomains is achieved, whereas all defects are annihilated before $t < 10^5$. However, the perfect-ordering process is done until $t \approx 3 \times 10^5$ for $\langle 40 \rangle$. According to this tendency, we can

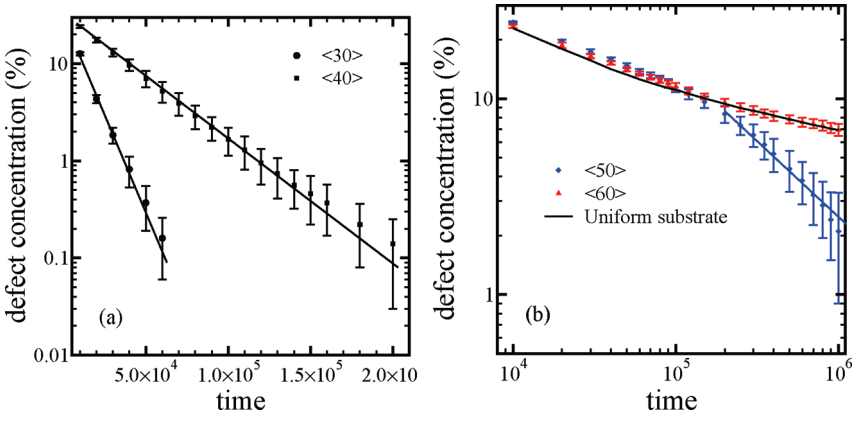

Figure 4. Time evolutions of the defect concentrations of the cylinders formed on field-patterned substrates. Note that (a) $L_s/L_0 = 3$ and 4 are plotted in a logorithmic-linear form and (b) $L_s/L_0 = 5$ and 6 are plotted in a double-logorithmic form together with the result of the uniform substrate.

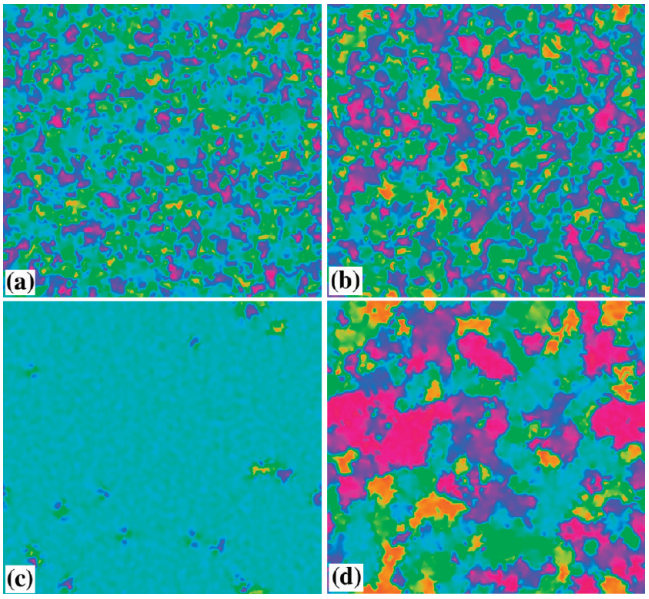

Figure 5. Orientation distribution of block copolymer microdomains for ⟨40⟩ (left column) and for ⟨60⟩ (right column) at time $t = 10^4$ (upper row) and 10^5 (bottom row).

predict that the perfect-ordering time must be very short when $L_s/L_0 = 2$ or $L_s/L_0 = \sqrt{3}$. It has been proven in our simulations that the time is shorter than 2×10^4 for ⟨20⟩, and this is the reason that its $f_{DF}(t)$ is not given in Figure 4a. When L_s/L_0 is increased to be larger than 4, such as 5 and 6, the relation of the exponential decay can no longer be observed in Figure 4b. The $f_{DF}(t)$ for ⟨50⟩ has a similar power law as that on the uniform substrate at the short time and has a power law with an exponent of ~0.62 for the long time. For ⟨60⟩, the $f_{DF}(t)$ on the whole time scale is quite similar to that on the uniform substrate.

In chemical-patterned films, the areas of potential wells attract A component to form cylinders quickly; then, these early formed cylinders with fixed positions act as soft confinement to their neighbor cylinders. The confinement can help other "free" cylinders to be arranged according to the orientation of the potential-well lattice. When the potential wells are denser ($L_s/L_0 \leq 4$), the confinement from earlier formed cylinders has stronger influence on the arranging of "free" cylinders. In addition, according to the coarsening mechanisms given by refs 15 and 16, the slowing down of the coarsening process is induced by the formation of polycrystalline grains, which are delimited by lines of dislocations with a pair of 5 and 7 coordinated-cylinder defects. It is pointed out that the average distance D_{DL} between neighbor dislocations is $\sim 2.5L_0$. This indicates that only single dislocation or a couple of dislocations can be formed locally at the initial quenching stage when $L_s/L_0 \leq 4$. Small grains without long dislocation-connected grain boundaries are easy to be annihilated by thermal fluctuations during the temporal evolution because of the high interfacial energy penalty. When the field patterns become sparse, that is, $L_s \geq 2D_{DL}$, more dislocations can be formed locally. This allows large grains with mismatched orientations to form. When these grains grow larger than their critical nucleation size, they continue growing and thus can be hardly annihilated by thermal fluctuations. The exponential decay of the defect concentration for $L_s/L_0 \leq 4$ can be derived from a phenomenological model. As the BCP domain lattice is divided into small pieces by the potential wells, it can be coarse-grained as a continuous and uniform system for the defect evolution. Therefore, the defect annihilating dynamics depends on its local density, $-dn_{DF}(\mathbf{r}, t)\, dt \propto n_{DF}(\mathbf{r}, t)$. With the assumption of uniformity on the coarse-grained scale, we can obtain $n_{DF}(t) \approx \exp(-Ct)$,

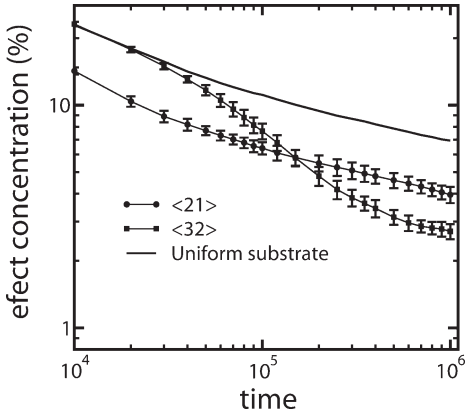

Figure 6. Time evolutions of the defect concentrations for two field patterns of ⟨21⟩ and ⟨32⟩. The decimal values of L_s/L_0 used by us are $L_s/L_0 = 2.646$ and $L_s/L_0 = 4.360$ for ⟨21⟩ and ⟨32⟩, respectively.

where C is a constant. Figure 5 shows the typical orientation distributions of BCP domain array for ⟨40⟩ (left column) and for ⟨60⟩ at $t = 10^4$ (upper row) and 10^5 (bottom row). These red grains have mismatch orientations with that of the field pattern. We can see that the average size of red grains in Figure 5a of ⟨40⟩ is smaller than that in Figure 5b of ⟨60⟩. At time $t = 10^5$, the whole region in Figure 5c of ⟨40⟩ becomes nearly order with a low defect concentration (~1.7%). However, in Figure 5d of ⟨60⟩, some misoriented grains grow to be large, and the defect concentration is still as high as ~11.4%. The conclusion that perfect ordering can be achieved when $L_s/L_0 \leq 4$ is similar to the observations in experiments.[32] In experiments, large defect-free arrays are observed with $L_s/L_0 \leq 3$, not our $L_s/L_0 \leq 4$. The small discrepancy between our theoretical results and experimental results can be resulted by a small incommensurability between the field pattern and the BCP domain lattice, which can be hardly avoided by experiments. The tolerance of the incommensurability by the field-patterned film is discussed in the following paragraph.

We turn to examine the field-pattern lattice of ⟨ij⟩ with nonzero i and j. For this kind of field pattern, the exact spacing ratio, determined by $(i^2 + j^2 + ij)^{1/2}$, is not an integer; therefore, the induced BCP domain array has two candidate orientations relative to the field-pattern lattice. Only when $i = j$ are the two orientations of $\theta = 30$ and $-30°$ are equivalent. Two typical field-spot lattices of ⟨21⟩ ($L_s/L_0 = \sqrt{7}$ and $\theta = \pm 19.1°$) and ⟨32⟩ ($L_s/L_0 = \sqrt{19}$ and $\theta = \pm 23.4°$) are simulated here. In the simulations, decimal values of $L_s/L_0 = 2.646$ and 4.360 are used for ⟨21⟩ and ⟨32⟩, respectively. The dynamic evolution functions of the defect concentration of $f_{DF}(t)$ are shown in Figure 6. The result from the uniform substrate is given as a comparison (solid line). The function $f_{DF}(t)$ of ⟨21⟩ with lower initial value and higher final value is slower than that of ⟨32⟩. The field-pattern lattice of ⟨21⟩ with earlier formed cylinders at the potential wells and hence results in lower initial defect concentration than ⟨32⟩. The difference of the coarsening speed is due to the different mismatch angle between two kinds of grains in the two field-pattern lattices. The mismatch angle is 21.8° for ⟨21⟩ and 13.2° for ⟨32⟩. The dislocations on the grain boundary with larger mismatch angle have lower mobility. In addition, after a long time annihilating process, the system has higher defect concentration because of the shorter dislocation distance for larger mismatch angle according to the model of $D_{DL}/L_0 \approx 1/\theta$ in ref 16 (or $D_{DL}/L_0 \approx 1/\tan\theta$ in ref 15). The BCP microdomain array of ⟨21⟩ as well as its orientational distribution is present in Figure 7. Both kinds of large grains with two different orientations are commensurate with the field-pattern lattice. This is very similar to the observation of Figure 4a in ref 32, although our field-patterned films are different from their postpatterned films.

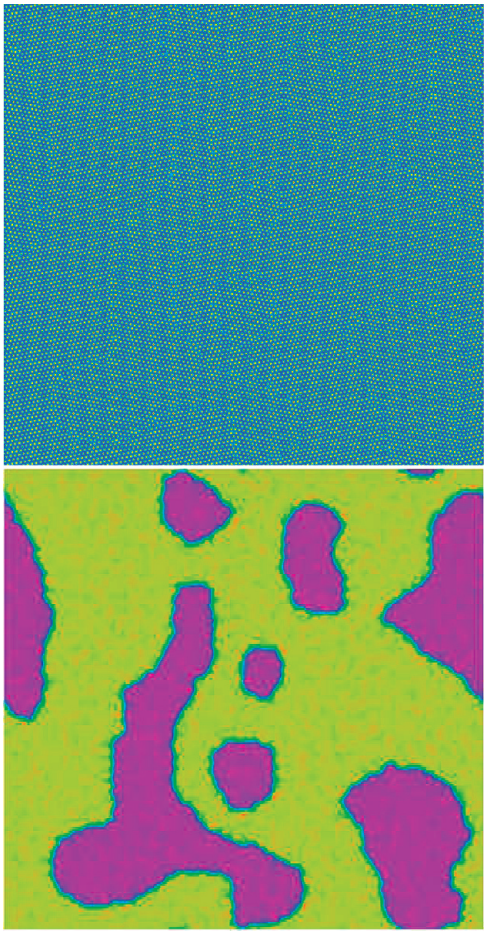

Figure 7. BCP microdomain array and its corresponding orientational distribution for ⟨21⟩. Red spots indicate the position centers of the field spots.

When preparing the field-pattern lattice, it is possible to introduce an incommensurability between the field-pattern lattice and the BCP domain lattice. How big incommensurability can be tolerated without breaking the long-range order is a interesting problem. Here we consider a small incommensurability in the pattern of ⟨20⟩ by making L_s/L_0 deviate from the integer of two. The dynamic functions of the defect concentrations for four values of L_s/L_0 = 1.90, 1.92, 2.08, and 2.10, which correspond to −5, −4, 4, and 5% deviations from 2 are shown in Figure 8. Only the time evolution of L_s/L_0 = 2.08 among the four evolution functions, whose curve looks close to a linear form, is fast-exponential decay. Compared with the case of L_s/L_0 = 2.08, that of L_s/L_0 = 1.92 has faster decay at short time, but it becomes much slower at long time. This suggests that it is possible to observe higher density defects in the patterned films with negative 4% than in those with positive 4% deviations from L_s/L_0 = 2. Similar phenomenon has been observed in the experimental work done by Tada et al.[30,31] In Figure 12 of ref 30, the BCP domains are perfectly ordered when the field pattern is commensurate with the domain lattice with L_s = 48 nm and L_0 = 24 nm. When the field-pattern spacing deviates from 48 to be 50 nm (about 2.08L_0) in Figure 13b of ref 30, the perfect-ordered BCP domains can still be formed. However, when L_s = 61 nm for L_0 = 32 nm ($L_s/L_0 \approx 1.91$), the ordering becomes obviously worse. (See Figure 11a of ref 30.) Even for L_s = 62 nm ($L_s/L_0 \approx 1.94$) in Figure 11b of ref 30, the ordering degree still looks worse than that of L_s/L_0 = 2.08 in Figure 13a,b of ref 30, where $L_s/L_0 \approx 1.96$, suggests that the orientation of the domain lattice is slightly distorted. In our calculations, we also carried a similar simulation with

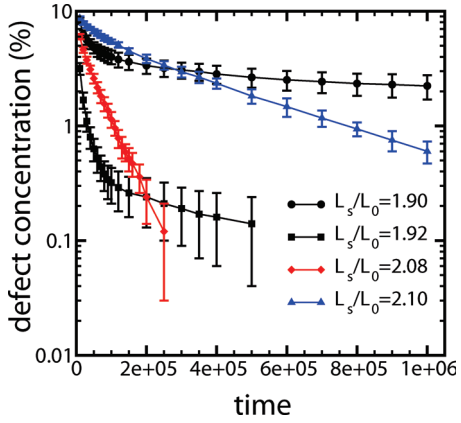

Figure 8. Time evolutions of the defect concentrations for the field pattern ⟨20⟩ with the lattice spacing L_s/L_0 deviating from the integer of two. The connected lines are just for the guide to eye.

L_s/L_0 = 1.96 (because the evolution time for perfect ordering is shorter than 2×10^4, we do not show the data), and we find that the BCP domains can be ordered perfectly. The comparison of results between L_s/L_0 = 1.96 and L_s/L_0 = 1.92 in our simulations indicates that the ordering process is quite sensitive to the magnitude of the incommensurability. This can explain why our results are different from that of experiments for L_s/L_0 = 1.96. The reason is that it is not ensured that L_s/L_0 is measured accurately in experiments. Small measurement error may result in a low-degree of imperfectness to the domain lattice. When the deviation is increased to be 5%, the long-range order is destroyed by the presence of >0.5% defects. The long-range order is determined by the competition between the surface interaction enthalpy and the entropic-energy penalty of BCP chains. When the deviation is small (<4%), the surface interaction dominates and makes the BCP chains be stretched or compressed to keep the domain lattice to match the field pattern. As the deviation becomes large (~5%), the entropic-energy penalty is comparable to the surface interaction enthalpy. The gross order of the domain lattice can still remain, but a few defects are formed to release part of the entropic-energy penalty. However, when the deviation is further increased (> 5%), the surface interaction cannot make up the loss of chain entropy, and polycrystalline grains are observed. Note that the tolerated critical deviation, breaking the long-range order, is much larger in experiments (~10%).[30] This is because the critical deviation depends on the multiple. In experiments, the results are for ⟨10⟩, and our results are for ⟨20⟩. It hints that the tolerated critical deviation decreases as the potential-well lattice becomes sparser. To check this point, we simulate the ⟨30⟩ field-patterned film. In this system, we find the appearance of an imperfectness when L_s/L_0 = 3.05. In very recent experiments,[31] Tada et al. observed considerable defects for the case of nine-fold multiplication when $L_s/L_0 = 3 \pm 0.08$. In their results, the regularity of positive deviation of L_s/L_0 = 3.08 is better than that of negative deviation of L_s/L_0 = 2.92. This is consistent with our results qualitatively.

IV. Conclusions

In summary, we have performed large-scale simulations on the ordering dynamics of the BCP microdomain formation in the field-patterned films by using cell dynamics simulations. The time evolutions of defect concentrations are used to measure the ordering dynamics of the BCP domains. First, we studied the effect of field patterns ⟨i0⟩ with i = 3, 4, 5, 6. By comparing their time evolutions of the defect concentrations, we find that perfect ordering can be achieved when $L_s/L_0 \leq 4$. Then, we carried examinations on ⟨ij⟩ field-patterned films with $i \times j \neq 0$. For this

kind of field pattern, we observed the formation of large polycrystalline grains with two lattice orientations. Finally, we investigated the tolerance of the incommensurability between the field-pattern lattice and the domain lattice for the case of $\langle i0 \rangle$. We find that the tolerance of incommensurability for the formation of perfect ordering depends sensitively on the spacing of the field patterns. For $\langle 20 \rangle$, the perfect ordering of BCP domains can be kept when the deviation of L_s/L_0 is $< 4\%$.

To focus on the influence of the chemical-field pattern on the formation of BCP microdomains, we simplify the films to a 2D system without considering the thickness effect. When the thickness of thin films is appropriate for perpendicular-cylinder formation, this simplification is valid. Because the size of our simulated films is as large as micrometers by micrometers, our results are helpful to understand available experimental observations. In addition to diblock copolymers, because the free energy functional used here can describe a wide variety of systems with strong wavelength selectivity, such as Langmuir films ferrofluids or magnetic garnets,[44] the results can be used to predict the dynamic behaviors in these systems.

Acknowledgment. This work was supported by the National Natural Science Foundation of China (grants 20974026, 20990231, 20625413). W.L. gratefully acknowledges supports from the Shanghai Pujiang Program (programs no. 08PJ1402000) and the Shanghai Educational Development Foundation.

References and Notes

(1) Park, M.; Harison, C.; Chaikin, P. M.; Register, R. A.; Adamson, D. H. *Science* **1997**, *276*, 1401.
(2) Lammertink, R. G. H.; Hempenius; van den Enk, J. E.; Chan, V. Z. H.; Thomas, E. L.; Vancso, G. J. *Adv. Mater.* **2000**, *12*, 98.
(3) Thurn-Albrecht, T.; Schotter, J.; Kastle, C. A.; Emley, N.; Shibauchi, T.; Krusin-Elbaum, L.; Guarini, K.; Black, C. T.; Tuominen, M. T.; Russell, T. P. *Science* **2000**, *290*, 2126.
(4) Park, M.; Chaikin, P. M.; Register, R. A.; Adamson, D. H. *Appl. Phys. Lett.* **2001**, *79*, 257.
(5) Black, C. T.; Guarini, K. W.; Milkove, K. R.; Baker, S. M.; Russell, T. P.; Tuominen, M. T. *Appl. Phys. Lett.* **2001**, *79*, 409.
(6) Cheng, J. Y.; Ross, C. A.; Chan, V. Z. H.; Thomas, E. L.; Lammertink, R. G. H.; Vancso, G. J. *Adv. Mater.* **2001**, *13*, 1174.
(7) Park, C.; Yoon, J.; Thomas, E. L. *Polymer* **2003**, *44*, 6725.
(8) Jung, Y. S.; Ross, C. A. *Nano Lett.* **2007**, *7*, 2046.
(9) Bates, F. S.; Fredrickson, G. H. *Annu. Rev. Phys. Chem.* **1990**, *41*, 525.
(10) Harrison, C. K.; Adamson, D. H.; Cheng, Z.; Sebastian, J. M.; Sethuraman, S.; Huse, D. A.; Register, R. A.; Chaikin, P. M. *Science* **2000**, *290*, 1558.
(11) Huang, Z. F.; Vinals, J. *Phys. Rev. E.* **2005**, *71*, 031501.
(12) Huang, Z. F.; Vinals, J. *Phys. Rev. E.* **2007**, *75*, 056202.
(13) Vinals, J. *J. Phys. Soc. Jpn.* **2009**, *78*, 041011.
(14) Harrison, C. K.; Cheng, Z.; Sethuraman, S.; Huse, D. A.; Chaikin, P. M.; Vega, D. A.; Sebastian, J. M.; Register, R. A.; Adamson, D. H. *Phys. Rev. E.* **2002**, *66*, 011706.
(15) Harrison, C. K.; Angelescu, D. E.; Trawick, M.; Cheng, Z.; Huse, D. A.; Chaikin, P. M.; Vega, D. A.; Sebastian, J. M.; Register, R. A.; Adamson, D. H. *Europhys. Lett.* **2004**, *67*, 800.
(16) Vega, D. A.; Harrison, C. K.; Angelescu, D. E.; Trawick, M. L.; Huse, D. A.; Chaikin, P. M.; Register, R. A. *Phys. Rev. E.* **2005**, *71*, 061803.
(17) Gomez, L. R.; Valles, E. M.; Vega, D. A. *Phys. Rev. Lett.* **2006**, *97*, 188302.
(18) Keller, A.; Pedemont, E.; Willmout, F. M. *Nature* **1970**, *225*, 538.
(19) Hashimoto, T.; Bodycomb, J.; Funaki, Y.; Kimishima, K. *Macromolecules* **1999**, *32*, 952.
(20) Berry, B. C.; Bosse, A. W.; Douglas, J. F.; Jones, R. L.; Karim, A. *Nano Lett.* **2007**, *7*, 2789.
(21) Kim, S. H.; Misner, M. J.; Russell, T. P. *Adv. Mater.* **2004**, *16*, 2119.
(22) Hashimoto, T.; Ogawa, T.; Sakamoto, N.; Ichimiya, M.; Kim, J. K.; Han, C. D. *Polymer* **1998**, *39*, 1573.
(23) Segalman, R. A.; Yokoyama, H.; Kramer, E. J. *Adv. Mater.* **2001**, *13*, 1152.
(24) Cheng, J. Y.; Ross, C. A.; Thomas, E. L.; Smith, H. I.; Vansco, G. J. *Appl. Phys. Lett.* **2002**, *81*, 3657.
(25) Cheng, J. Y.; Mayes, A. M.; Ross, C. A. *Nat. Mater.* **2004**, *3*, 823.
(26) Kim, S. O.; Solak, H. H.; Stoykovich, M. P.; Ferrier, N. J.; de Pablo, J. J.; Nealey, P. F. *Nature* **2003**, *424*, 411.
(27) StoyKovich, M. P.; Muller, M.; Kim, S. O.; Edwards, E. W.; de Pablo, J. J.; Nealey, P. F. *Science* **2005**, *308*, 5727.
(28) Ruiz, R.; Kang, H.; Detcheverry, F. A.; Dobisz, E.; Kercher, D. S.; Albrecht, T. R.; de Pablo, J. J.; Nealey, P. F. *Science* **2008**, *321*, 936.
(29) Cheng, J. Y.; Rettner, C. T.; Sanders, D. P.; Kim, H. C.; Hinsberg, W. D. *Adv. Mater.* **2008**, *20*, 3155.
(30) Tada, Y.; Akasaka, S.; Yoshida, H.; Hasegawa, H.; Dobisz, E.; Kercher, D.; Takenaka, M. *Macromolecules* **2008**, *41*, 9267.
(31) Tada, Y.; Akasaka, S.; Takenaka, M.; Yoshida, H.; Ruiz, R.; Dobisz, E.; Hasegawa, H. *Polymer* **2009**, *50*, 4250.
(32) Bita, I.; Yang, J. K. W.; Jung, Y. S.; Ross, C. A.; Thomas, E. L.; Berggren, K. K. *Science* **2008**, *321*, 939.
(33) Wang, Q.; Nealey, P. F.; de Pablo, J. J. *Macromolecules* **2003**, *36*, 1731.
(34) Edwards, E. W.; Muller, M.; Stoykovich, M. P.; Solak, H. H.; de Pablo, J. J.; Nealey, P. F. *Macromolecules* **2007**, *40*, 90.
(35) Oono, Y.; Puri, S. *Phys. Rev. Lett.* **1987**, *58*, 836.
(36) Oono, Y.; Puri, S. *Phys. Rev. A* **1988**, *38*, 434.
(37) Puri, S.; Oono, Y. *Phys. Rev. A* **1988**, *38*, 1542.
(38) Groot, R. D.; Madden, T. J. *J. Chem. Phys.* **1998**, *108*, 8713.
(39) Fraaije, J. G. E. M. *J. Chem. Phys.* **1993**, *99*, 9202.
(40) Cahn, J. W. *Acta Metall.* **1961**, *9*, 795.
(41) Ohta, T.; Kawasaki, K. *Macromolecules* **1986**, *19*, 2621.
(42) Yokojima, Y.; Shiwa, Y. *Phys. Rev. E* **2002**, *65*, 056308.
(43) Bray, A. J. *Adv. Phys.* **2002**, *51*, 481–587.
(44) Seul, M.; Andelman, D. *Science* **1995**, *267*, 476.